



ORIGINAL ARTICLE

Fuzuli Ağrı Akçay · Erkan Oterkus

A criterion for dynamic ductile fracture initiation of tensile mode

Received: 12 October 2020 / Accepted: 30 January 2021 / Published online: 22 February 2021
© The Author(s), under exclusive licence to Springer-Verlag GmbH, DE part of Springer Nature 2021

Abstract Dynamic behavior of a material is essential in applications such as collision, explosion, ballistic impact, high-speed machining, and metal forming. As impact loadings, as well as accidental or malicious explosions, may impose high loading rates to engineering structures, estimating the dynamic response of a material accurately is crucial. Therefore, an analytical strain rate-dependent criterion on ductile fracture initiation is developed at the continuum scale by further developing the energy balance concept. The criterion is based on continuum modeling of energy release rates, and the critical state is reached when the rate of energy change of fractured and unfractured states becomes equal. The formulation introduces a material length scale and a material property that is a function of strain rate and temperature. The developed ductile fracture criterion is implemented into two example applications, an aluminum alloy and a titanium alloy, whose experimental data are obtained from the open literature. Fracture loci of these alloys at various strain rates and the critical energy release rates as a function of strain rate are determined. The results of the example applications agree well with the experimental results reported in the literature.

Keywords Fracture · Ductility · Strain rate dependent · Plasticity · Energy release rate

Nomenclature

A	Area of the fracture plane
A_1, A_2, A_3	Material constants
c_V	Specific heat capacity at constant volume
C_I	Specific surface energy density
du	Plastic work increment per unit volume
dk	Kinetic energy increment per unit volume
dW	Mechanical work increment per unit volume (of the unfractured medium)
dW	Mechanical work increment of the unfractured medium
dW^*	Mechanical work increment of the fractured medium
$d\varepsilon_{ij}$	Components of (plastic) strain increment tensor (of the unfractured medium)
$d\varepsilon_I, d\varepsilon_{II}, d\varepsilon_{III}$	Strain increments of the unfractured medium in principal directions
$d\varepsilon_I^*, d\varepsilon_{II}^*, d\varepsilon_{III}^*$	Strain increments of the fractured medium in principal directions

Communicated by Marcus Aßmus and Andreas Öchsner.

F. A. Akçay (✉)
İstanbul Teknik Üniversitesi Gemi İnşaatı ve Deniz Bilimleri Fakültesi, Maslak, İstanbul 34469, Turkey
E-mail: akcayfu@itu.edu.tr

E. Oterkus
Department of Naval Architecture, Ocean and Marine Engineering, University of Strathclyde, Glasgow G4 0LZ, UK

$d\varepsilon_{\text{eff}}$	Equivalent (plastic) strain increment
$l_{I,0}$	Characteristic length (relevant to ductile fracture)
l_I, l_{II}, l_{III}	Current dimensions of the volume element
m, n	Material constants
T	Actual material temperature
T_{melt}	Melting temperature of the material
T_{room}	Room temperature
v_I, v_{II}, v_{III}	Components of velocity vector (in principal directions)
x_I, x_{II}, x_{III}	Principal directions
β	Fraction of the plastic work contributing to temperature increase
ε_{ij}	Components of true strain
$\dot{\varepsilon}_0$	Reference strain rate
$\dot{\varepsilon}_I, \dot{\varepsilon}_{II}, \dot{\varepsilon}_{III}$	True strain rates in principal directions
ε_{eff}	Equivalent (plastic) strain
$\bar{\varepsilon}_f$	Equivalent (plastic) strain at fracture
λ	Nonnegative scalar factor
ρ	Mass density of the material
σ_{ij}	Components of true stress tensor
$\sigma_I, \sigma_{II}, \sigma_{III}$	Principal stresses of the unfractured medium
$\sigma_I^*, \sigma_{II}^*, \sigma_{III}^*$	Principal stresses of the fractured medium
σ_{eff}	Equivalent stress
Γ_I	Critical effective energy release rate (of tensile mode fracture)
ΔT	Increase in temperature

1 Introduction

Impact loadings, as well as accidental or malicious explosions, may impose high loading rates to engineering structures [36]. Therefore, dynamic behavior of a material, which can significantly differ from its static one [8], is essential in applications such as collision, explosion, ballistic impact, high-speed machining, and metal forming. As the choice of the constitutive model and the identification of model parameters are vital [72], a large number of research studies that investigated the dynamic response of materials focused on establishing a plastic constitutive model. Plastic constitutive models can be divided into two categories: Microstructure-based physical models and empirical phenomenological models [50]. In addition, plastic constitutive models can be categorized as rate-independent models or rate-dependent models. Interested readers on rate-independent constitutive models are referred to recent articles by Siddiq [83], Asim et al. [5], and Fu et al. [32]. On the other hand, rate-dependent constitutive models are discussed more in detail in the following paragraphs.

Zerilli and Armstrong [101] model is an example of microstructure-based physical model. The model is based on dislocation mechanics and the constitutive equations were developed for body-centered-cubic (BCC) and face-centered-cubic (FCC) materials. Later, Voyiadjis and Abed [95] discussed the derivation of Zerilli–Armstrong constitutive equations and they proposed a model that accounts for the evolution of mobile dislocation density. Various models that consider the effect of dislocation density evolution on the response of different crystal structures are available in the literature (see, e.g., [7, 34, 52, 80, 81, 94]). A widespread use of microstructure-based physical models is limited, as they generally involve a large number of parameters [85].

An example of empirical phenomenological model is Johnson and Cook [43] model. Johnson and Cook [43] presented a constitutive model that primarily aims to ease numerical implementation. The model includes five material constants, and the authors provided the numerical values of these constants for twelve different materials. Another example of empirical phenomenological model was proposed by Khan and Liang [48] based on the experimental results of three BCC metals (tantalum, tantalum alloy with 2.5% tungsten, and AerMet 100 steel). This model has been subjected to several modifications based on the observations on the mechanical responses of polycrystalline materials during nearly two decades [45, 50]. In addition to those mentioned, numerous phenomenological models have been proposed in the literature (see, e.g., [65, 82, 92]). Interested readers are referred to Sung et al. [89], Huh et al. [42], and Tanimura et al. [90], where a summary and comparison of several strain rate (and temperature)-dependent constitutive models are presented.

Material failure models can be divided into physically based models and empirical phenomenological models as well. Additionally, they can be divided into two categories as coupled models and uncoupled models.

The former approach couples the constitutive model and the fracture criterion, that is, damage accumulation is incorporated into the constitutive model. A well-known example of this class is the Gurson model [37]. Gurson model, developed for porous ductile materials, is based on the void growth mechanics and has been subjected to modifications to account for realistic values (see, e.g., [91]) as well as shear dominated stress states (see, e.g., [67] for shear modification and [69] for further extension). Interested readers are referred to Benzerga et al. [11] for a comprehensive review of Gurson-based models. Moreover, variational methods have been utilized as well in order to model damage accumulation (see, e.g., [75–77,84]). On the other hand, the latter approach decouples damage accumulation and the constitutive model, that is, fracture criterion and the constitutive model act independent from each other. Hancock–Mackenzie model [40] can be given as an example for this class.

In contrast to the plastic constitutive models, only a small portion of studies (that investigated the dynamic response of materials) focused on establishing a ductile fracture criterion for dynamic loading conditions. More than three decades ago, Johnson and Cook [44] proposed a strain rate (and temperature)-dependent fracture criterion based on the results of a series of tensile tests on three different metals (OFHC copper, Armco iron, and 4340 steel). Although the original version is still used in the literature, Johnson–Cook fracture model has been exposed to modifications as well (see, e.g., [15]). Other strain rate-dependent ductile fracture criteria have been proposed in addition to Johnson–Cook-based failure criteria. Kim et al. [54] proposed two failure criteria (using the effective strain or damage parameters) as a function of Zener–Holloman parameter [100] to predict the fracture behavior of magnesium alloy sheets. The proposed criteria are based on observations and deep drawing experiments of AZ31 sheets were conducted in order to validate the proposed criteria. Khan and Liu [51] proposed an empirical strain rate (and temperature)-dependent fracture criterion, based on the magnitude of stress vector criterion [49], and the criterion was calibrated for Al2024–T351 alloy. Liu and Sun [59] proposed a dynamic ductile fracture model that involves the effect of hydrostatic pressure, Lode angle, and the strain rate. The criterion was applied to determine the material parameters of Al–7075 alloy. Roth and Mohr [79] proposed an empirical extension of the Hosford–Coulomb model [63] to include the strain rate effect on fracture initiation. The expression was calibrated and validated using the experimental results of DP590 steel and TRIP780 steel. Although a comprehensive review on dynamic ductile fracture lacks, interested readers are referred to Molinari et al. [64] for dynamic necking and fragmentation, and dynamic damage by microvoiding with applications to spalling and dynamic crack growth.

Currently, the original [44] or slightly modified versions (see, e.g., [15]) of Johnson–Cook fracture criterion is commonly used to account for the effect of strain rate (and temperature). However, Johnson–Cook fracture criterion and its modifications experience fundamental shortcomings as presented in the following. Firstly, Johnson–Cook criterion is based on stress triaxiality only; therefore, it cannot capture the difference between different stress states of same triaxiality. Nevertheless, experimental studies have shown that the Lode angle/parameter (that is, the third stress invariant) plays an important role (in addition to stress triaxiality) in ductile fracture process (see, e.g., [9,10,20,97]). Hence, both parameters need to be taken into account to predict ductile fracture accurately. Although researchers have modified Johnson–Cook criterion in order to include the Lode angle dependency, this results in extra material constant(s), which requires additional experiment(s) to calculate these new constant(s) (see, e.g., [29]). Secondly, Johnson–Cook fracture criterion exhibits mesh size dependency [56]. Thirdly, Johnson–Cook-based fracture criteria as well as aforementioned fracture criteria are empirical, and an analytical strain rate-dependent ductile fracture criterion still lacks. Therefore, the aim of the current study is to develop an analytical strain rate-dependent criterion on ductile fracture initiation at the continuum scale. This relationship is obtained by further developing the energy balance concept [47]. The energy-based criterion to be developed includes the stress triaxiality and the Lode angle dependencies inherently, without the necessity of extra material constants, by considering the stress state as a whole. Moreover, as the criterion to be developed introduces a characteristic length, use of characteristic length as a mesh size removes mesh dependency. The novelty of the current research is development of a rate-dependent ductile fracture criterion (of tensile mode) that is physically based, mesh independent and encompasses stress triaxiality and Lode angle/parameter dependencies inherently.

Dynamic loading here and thereafter corresponds to non-cyclic loading cases, that is, fatigue loading is beyond the scope of the current investigation and studied elsewhere (see, e.g., [3,4,58,68]). The article is organized as follows. The ductile fracture criterion is derived in Sect. 2, and implemented into two example applications in Sect. 3. The results are presented and discussed in Sect. 4. Finally, a summary with conclusion remarks are given in Sect. 5.

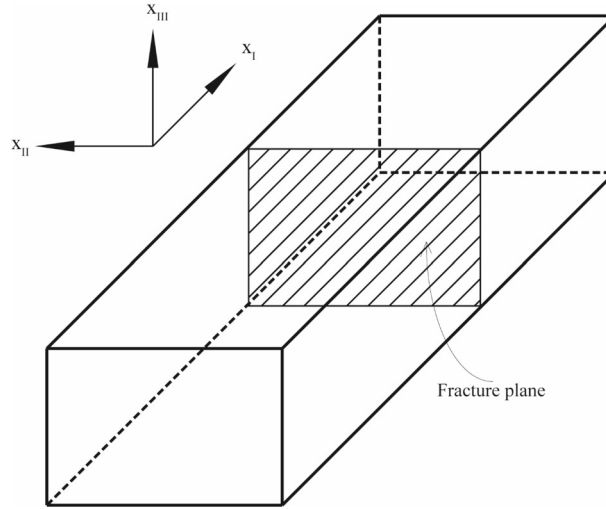


Fig. 1 Volume element and potential fracture plane

2 Ductile fracture criterion for dynamic loading

In this section, an analytical strain rate-dependent criterion on ductile fracture initiation at the continuum scale is developed. This relationship is obtained by further developing the energy balance concept [47] and the focus is given only tensile mode (i.e., Mode I) fracture.

Conservation of energy principle requires the sum of the rate of work done on a body by external forces and all other energy rates being equal to the time rate of change of the internal energy and the kinetic energy [31]. In the following, the case where the work done on the system is only by external forces is considered, that is, no other external energy enters the system. It is also assumed that there are no pre-existing cracks or damage at the continuum scale. Moreover, elastic deformation (i.e., elastic strain energy) can be ignored as ductile fracture usually associated with large strains where plastic deformation dominates. The mechanical work increment per unit volume, dw , then takes the form of

$$dw = du + dk = \sigma_{ij}d\varepsilon_{ij} + \rho v_i dv_i \quad (1)$$

where du and dk represent the plastic work increment and the kinetic energy increment per unit volume, respectively. Also, σ_{ij} are the components of true stress tensor, $d\varepsilon_{ij}$ are the components of (plastic) strain increment tensor, ρ is the mass density of the material, and v_i are the components of velocity vector.

Let consider an isotropic continuous medium in a rectangular Cartesian coordinate system subjected to uniform state of stress before fracture. Suppose that this medium has the current dimensions of l_I , l_{II} , and l_{III} in the principal directions of x_I , x_{II} , and x_{III} , respectively. The volume element with a potential fracture plane is presented in Fig. 1.

The mechanical work increment per unit volume of the unfractured medium can be written in terms of principal values as

$$dw = \sigma_I d\varepsilon_I + \sigma_{II} d\varepsilon_{II} + \sigma_{III} d\varepsilon_{III} + \rho (v_I dv_I + v_{II} dv_{II} + v_{III} dv_{III}) \quad (2)$$

where $\sigma_I \geq \sigma_{II} \geq \sigma_{III}$. Also, the natural strain components in the principal directions are defined as

$$d\varepsilon_I = dl_I/l_I, d\varepsilon_{II} = dl_{II}/l_{II}, d\varepsilon_{III} = dl_{III}/l_{III}. \quad (3)$$

Integrating Eq. (3) yields

$$\varepsilon_I = \ln \frac{l_I}{l_{I,0}}, \varepsilon_{II} = \ln \frac{l_{II}}{l_{II,0}}, \varepsilon_{III} = \ln \frac{l_{III}}{l_{III,0}} \quad (4)$$

where $l_{i,0}$ and l_i are the initial and the current length components of the volume element, respectively. Now, let take the time derivative of Eq. (4)

$$\dot{\varepsilon}_I = \frac{1}{l_I} \frac{dl_I}{dt}, \dot{\varepsilon}_{II} = \frac{1}{l_{II}} \frac{dl_{II}}{dt}, \dot{\varepsilon}_{III} = \frac{1}{l_{III}} \frac{dl_{III}}{dt} \quad (5)$$

where $\dot{\varepsilon}_I$, $\dot{\varepsilon}_{II}$, $\dot{\varepsilon}_{III}$ are the true strain rates in the principal directions.

Rigid body translational or rotational velocities are not considered (in the calculation of kinetic energy increment) as they do not make any contribution to fracture process. In other words, the 'effective/active' velocity is $v_i = dl_i/dt$ not $v_i = dx_i/dt$, with x_i representing the components of position vector. Hence, the velocity components can simply be written as

$$v_I = l_I \dot{\varepsilon}_I, v_{II} = l_{II} \dot{\varepsilon}_{II}, v_{III} = l_{III} \dot{\varepsilon}_{III}. \quad (6)$$

Equation (6) is in accordance with the true strain rate definition given by Dieter [26]. Differentiating both sides of Eq. (6) yields

$$\begin{aligned} dv_I &= l_I d\dot{\varepsilon}_I + \dot{\varepsilon}_I dl_I \\ dv_{II} &= l_{II} d\dot{\varepsilon}_{II} + \dot{\varepsilon}_{II} dl_{II} \\ dv_{III} &= l_{III} d\dot{\varepsilon}_{III} + \dot{\varepsilon}_{III} dl_{III}. \end{aligned} \quad (7)$$

It is presumed that the strain rate remains nearly constant during an increment, that is, $d\dot{\varepsilon}_I = d\dot{\varepsilon}_{II} = d\dot{\varepsilon}_{III} = 0$. Hence, Eq. (7) reduces to

$$dv_I = \dot{\varepsilon}_I dl_I, dv_{II} = \dot{\varepsilon}_{II} dl_{II}, dv_{III} = \dot{\varepsilon}_{III} dl_{III}. \quad (8)$$

Substituting Eq. (3) into Eq. (8) yields

$$dv_I = l_I \dot{\varepsilon}_I d\varepsilon_I, dv_{II} = l_{II} \dot{\varepsilon}_{II} d\varepsilon_{II}, dv_{III} = l_{III} \dot{\varepsilon}_{III} d\varepsilon_{III}. \quad (9)$$

Finally, substituting Eqs. (6) and (9) into Eq. (2), and multiplying by the current volume yield the mechanical work increment of the unfractured medium, dW

$$dW = l_I l_{II} l_{III} \left\{ [\sigma_I + \rho (l_I \dot{\varepsilon}_I)^2] d\varepsilon_I + [\sigma_{II} + \rho (l_{II} \dot{\varepsilon}_{II})^2] d\varepsilon_{II} + [\sigma_{III} + \rho (l_{III} \dot{\varepsilon}_{III})^2] d\varepsilon_{III} \right\}. \quad (10)$$

This expression, i.e., Eq. (10), provides the necessary amount of energy increment for the system to deform without fracture; that is, dE . On the other hand, the necessary amount of energy increment for the system to fracture, dE^* , includes an additional energy that is required to create new surfaces [47], that is

$$dE^* = (\Gamma_I \times A) d\varepsilon_I + dW^* \quad (11)$$

where

$$dW^* = l_I l_{II} l_{III} \left\{ \left[\sigma_I^* + \rho (l_I \dot{\varepsilon}_I^*)^2 \right] d\varepsilon_I^* + \left[\sigma_{II}^* + \rho (l_{II} \dot{\varepsilon}_{II}^*)^2 \right] d\varepsilon_{II}^* + \left[\sigma_{III}^* + \rho (l_{III} \dot{\varepsilon}_{III}^*)^2 \right] d\varepsilon_{III}^* \right\}. \quad (12)$$

Here, Γ_I denotes the critical effective energy release rate per unit surface area of the fracture plane (of tensile mode fracture) and dW^* is the mechanical work increment of the fractured medium. Tensile mode fracture plane and its area, which is $A = l_{II} l_{III}$, are shown in Fig. 1. Also, all stress, strain, and strain rate quantities denoted by star are associated with the fractured medium. Moreover, the critical effective energy release rate (Γ) is a material property for a particular fracture mode [47], and it can be a function of strain rate and temperature.

The rate of energy change of the unfractured medium is initially less than the fractured medium, as the system maintains the minimum energy state. In other words, the system, seeking the minimum energy state, will fracture if the necessary energy increment for the fractured state becomes less than the necessary energy increment for the unfractured state. Therefore, the critical state is reached when the rate of energy change of these two states becomes equal [47]. Hence, mathematical representation of the critical state is

$$dE = dE^* \quad (13)$$

with principal stresses and strains, and strain rates maintained consistent with the boundary conditions, that is

$$\begin{aligned} \sigma_{II}^* d\varepsilon_{II}^* &= \sigma_{II} d\varepsilon_{II}, \left(\dot{\varepsilon}_{II}^* \right)^2 d\varepsilon_{II}^* = (\dot{\varepsilon}_{II})^2 d\varepsilon_{II} \\ \sigma_{III}^* d\varepsilon_{III}^* &= \sigma_{III} d\varepsilon_{III}, \left(\dot{\varepsilon}_{III}^* \right)^2 d\varepsilon_{III}^* = (\dot{\varepsilon}_{III})^2 d\varepsilon_{III}. \end{aligned} \quad (14)$$

As the increment in strain is concentrated in the fracture zone, $d\varepsilon_I^*$ suddenly drops to zero; hence, the first term (in the parenthesis) of Eq. (12) vanishes. Therefore, the critical state condition, i.e., Eq. (13), takes the following form

$$l_I l_{II} l_{III} [\sigma_I + \rho (l_I \dot{\varepsilon}_I)^2] d\varepsilon_I = (\Gamma_I \times A) d\varepsilon_I. \quad (15)$$

Substituting $A = l_{II} l_{III}$ into Eq. (15) and simplifying it yields

$$l_I [\sigma_I + \rho (l_I \dot{\varepsilon}_I)^2] = \Gamma_I. \quad (16)$$

Now, let define

$$C_I = \frac{\Gamma_I}{l_{I,0}}. \quad (17)$$

Finally, substituting Eqs. (4) and (17) into Eq. (16) yields the critical state for tensile mode fracture

$$e^{\varepsilon_I} [\sigma_I + \rho (l_I \dot{\varepsilon}_I)^2] = C_I. \quad (18)$$

As presented above, $l_{I,0}$ and l_I are the initial and the current length of the volume element, respectively, in the maximum principal stress/strain direction. Use of a material feature (e.g., a characteristic length) for $l_{I,0}$ such that the stress state within the volume element remains uniform at the continuum scale is suggested. Hence, in this case, C_I is a material property, and can be a function of strain rate and temperature. Physically, C_I represents the specific surface energy density as it refers to critical effective energy release rate per unit (characteristic) length [47].

The critical state condition given by Eq. (18) does not include any terms that take the history of state of stress or strain into consideration. Hence, this form of the equation is suggested to be utilized for proportional loading conditions. On the other hand, a slight improvement to Eq. (18) that can be used for non-proportional loading cases is proposed in the following

$$e^{\int_0^{\varepsilon_{eq}} (1/\zeta_I) d\varepsilon_{eq}} [\sigma_I + \rho (l_I \dot{\varepsilon}_I)^2] = C_I \quad (19)$$

where

$$\zeta_I = \sqrt{\frac{2}{3} \left[1 + \left(\frac{d\varepsilon_{II}}{d\varepsilon_I} \right)^2 + \left(\frac{d\varepsilon_{III}}{d\varepsilon_I} \right)^2 \right]} \quad (20)$$

$$d\varepsilon_{eq} = \sqrt{\frac{2}{3} [(d\varepsilon_I)^2 + (d\varepsilon_{II})^2 + (d\varepsilon_{III})^2]}. \quad (21)$$

Here, plastic incompressibility is assumed and ζ_I is assumed to remain constant during an increment. $d\varepsilon_{eq}$ denotes the equivalent (plastic) strain increment with ε_{eq} denoting the equivalent (plastic) strain. The integral term in Eq. (19) takes the deformation history into account; hence, use of Eq. (19) is suggested for non-proportional loading cases. Accordingly, use of the integral term $\int_0^{\varepsilon_{eq}} (1/\zeta_I) d\varepsilon_{eq}$ is suggested in the graphical illustration of fracture locus (instead of equivalent plastic strain itself (ε_{eq})) for non-proportional loading cases. If the loading is proportional, ζ_I remains constant throughout loading and Eq. (19) reduces to Eq. (18).

There is not sufficient time for appreciable heat flow to occur at high rates of deformation [26] due to sudden and abrupt nature of the crack nucleation process [18]. Therefore, in high loading cases, where the plastic work cannot be totally dissipated, there will be temperature increase in the material. Although a temperature term does not explicitly appear in the critical state equation (Eq. 19), the effect of temperature increase should be included implicitly by determining the current temperature after each increment, and updating the values of temperature-dependent terms, particularly σ_I (i.e., the constitutive equations) and C_I , accordingly. The increase in temperature, ΔT , can be computed by

$$\Delta T = \frac{\beta}{\rho c_V} \int \sigma_{ij} d\varepsilon_{ij} \quad (22)$$

where β is the fraction of the plastic work contributing to temperature increase, and c_V is the specific heat capacity at constant volume. Here, the thermal energy term is considered to be only generated by mechanical work; however, extraneous heat sources may exist in the system that are not purely mechanical (see, e.g., Rittel, 2014 for details). Additionally, the reason for the use of the specific heat capacity at constant volume is that the plastic flow is essentially isochoric [46].

3 Example applications

Numerous experimental studies have been conducted in order to explore the effect of dynamic loading on fracture behavior of metals, including various types of steels [1,2,14,16,23,30,35,53,57,62,93], aluminum alloys [13,21,22,28,73,87], magnesium alloys [28,98], titanium alloys [12,28,41,96,102], nickel alloys [86], tungsten alloys [78], and tantalum [27]. In addition, fracture behavior of additively manufactured metals is a rising topic of research interest (see, e.g., [24,88,99]) thanks to rapid development of 3D-printing technology. However, in this section, the experimental results of Bobbili et al. [13] and Bobbili and Madhu [12] are utilized, as the articles were published recently and the authors provided enough data of interest (i.e., true fracture strain values for various stress states and strain rates) to investigate the application of the proposed criterion.

The von-Mises equivalent stress in terms of principal stresses is defined as

$$\sigma_{\text{eq}} = \sqrt{\frac{1}{2} [(\sigma_{\text{I}} - \sigma_{\text{II}})^2 + (\sigma_{\text{II}} - \sigma_{\text{III}})^2 + (\sigma_{\text{III}} - \sigma_{\text{I}})^2]}. \quad (23)$$

Also, for a given stress state, it is convenient to express the equivalent stress in terms of maximum principal stress, that is

$$\sigma_{\text{eq}} = \xi_{\text{I}} \sigma_{\text{I}} \quad (24)$$

with ξ_{I} takes the following form for the axisymmetric stress state [47]

$$\xi_{\text{I}} = \frac{3}{2 + 3\eta} \quad (25)$$

where η is the stress triaxiality.

Moreover, the flow rule is expressed as [25]

$$\begin{aligned} d\varepsilon_{\text{I}} &= \frac{2}{3} \lambda \left[\sigma_{\text{I}} - \frac{1}{2} (\sigma_{\text{II}} + \sigma_{\text{III}}) \right] \\ d\varepsilon_{\text{II}} &= \frac{2}{3} \lambda \left[\sigma_{\text{II}} - \frac{1}{2} (\sigma_{\text{I}} + \sigma_{\text{III}}) \right] \\ d\varepsilon_{\text{III}} &= \frac{2}{3} \lambda \left[\sigma_{\text{III}} - \frac{1}{2} (\sigma_{\text{I}} + \sigma_{\text{II}}) \right] \end{aligned} \quad (26)$$

where λ is a non-negative scalar factor and may vary throughout loading.

Bobbili et al. [13] and Bobbili and Madhu [12] conducted tensile tests on Al–4.8Cu–1.2Mg alloy and Ti–10V–2Fe–3Al alloy to investigate the fracture behavior of these alloys at different loading rates. They provided experimental data for four different stress triaxialities at four strain rates. However, as there was no explicit information on the fracture mode of the smooth specimens, only the data of notched specimens (i.e., three data points for each strain rate) are considered here, that is, $\eta = 0.5153$, $\eta = 0.6209$, and $\eta = 0.7387$. Moreover, the authors did not provide any data for strain rate beyond 1000 s^{-1} for Al–4.8Cu–1.2 Mg alloy and 1500 s^{-1} for Ti–10V–2Fe–3Al alloy. Hence, Johnson–Cook fracture criterion [44] is used to calculate the approximate fracture strains at any loading case beyond these strain rates. The fracture strain values at these loading cases are calculated for the same three stress triaxialities. Furthermore, although proportional loading is not generally the case in actual experiments, it is assumed that the stress triaxiality remains nearly constant throughout loading, as the authors did not provide any experimental data on the evolution of stress triaxiality. Hence, for the proportional loading case, as mentioned above, ζ_{I} remains constant throughout loading with $\zeta_{\text{I}} = 1$ for the axisymmetric case [47].

Johnson–Cook constitutive model [43] is used to represent the constitutive behavior of Al–4.8Cu–1.2Mg and Ti–10V–2Fe–3Al alloys, as Bobbili et al. [13] and Bobbili and Madhu [12] used Johnson–Cook constitutive model as well, and they provided the material constants of the model. The authors also proposed a slightly modified version of Johnson–Cook constitutive equation to improve the prediction accuracy of the flow behavior of the materials of interest at high strain rates and temperatures [12,13]. However, the original Johnson–Cook constitutive equation, given in the following, is used here as it describes the flow behavior of the materials of interest fairly well, as well.

$$\sigma_{\text{eq}} = \left[A_1 + A_2 \varepsilon_{\text{eq}}^n \right] \left[1 + A_3 \ln \left(\frac{\dot{\varepsilon}}{\dot{\varepsilon}_0} \right) \right] \left[1 - \left(\frac{T - T_{\text{room}}}{T_{\text{melt}} - T_{\text{room}}} \right)^m \right] \quad (27)$$

where σ_{eq} , ε_{eq} , $\dot{\varepsilon}$, and $\dot{\varepsilon}_0$ are the equivalent stress, equivalent plastic strain, strain rate, and reference strain rate, respectively. Also, T , T_{room} , and T_{melt} are the actual material temperature, room temperature and the melting temperature of the material, respectively. Moreover, there are five material constants (A_1 , A_2 , A_3 , n , m) to be determined. Different strategies on the calculation of these material parameters were extensively discussed by Gambirasio and Rizzi [33] and the material constants were determined for three materials (i.e., DH36 structural steel, a commercially pure niobium and an AL-6XN stainless steel) using the published experimental data.

3.1 Example 1: Tensile mode fracture of Al–4.8Cu–1.2Mg

Bobbili et al. [13] conducted tensile tests on Al–4.8Cu–1.2Mg alloy at four different strain rates: 0.01 s^{-1} , 0.1 s^{-1} , 1 s^{-1} , 1000 s^{-1} . Nevertheless, the specific surface energy density, C_I , is determined for three additional strain rates as well, i.e., for 5000 s^{-1} , $20,000 \text{ s}^{-1}$, $50,000 \text{ s}^{-1}$. The approximate fracture strains at these strain rates are calculated by using Johnson–Cook fracture criterion, given by Bobbili et al. [13] as

$$\bar{\varepsilon}_f = \left[0.05 + 1.281e^{-3.5\eta} \right] \left[1 + 0.138 \ln \left(\frac{\dot{\varepsilon}}{\dot{\varepsilon}_0} \right) \right]. \quad (28)$$

Again, as mentioned previously, Eq. (28) is used to determine the fracture strains only for three stress triaxialities in order to obtain the approximate value of C_I at strain rates beyond 1000 s^{-1} .

Moreover, the following constitutive equation, whose material constants are provided by Bobbili et al. [13], is used to predict the flow behavior of Al–4.8Cu–1.2Mg alloy

$$\sigma_{\text{eq}} = \left[380 + 482\varepsilon_{\text{eq}}^{0.51} \right] \left[1 + 0.0128 \ln \left(\frac{\dot{\varepsilon}}{\dot{\varepsilon}_0} \right) \right] \quad (29)$$

with the reference strain rate is taken as $\dot{\varepsilon}_0 = 1 \text{ s}^{-1}$.

There is no published data on mass density or average spacings of large inclusions of Al–4.8Cu–1.2Mg alloy, to the authors' best knowledge. Additionally, although the temper designation of the Al alloy is provided as T6, its commercial name is not known (personal communication with Dr. Bobbili through e-mail). However, the copper and magnesium contents of Al–4.8Cu–1.2Mg alloy remains within the chemical composition range of Al 2024 and Al 2124 alloys [19]. Therefore, properties of these two alloys are considered to approximate the mass density and characteristic length of Al–4.8Cu–1.2Mg alloy.

Mass densities of Al 2024 and Al 2124 alloys are 2770 kg/m^3 [6]; hence, the mass density of Al–4.8Cu–1.2Mg alloy is taken as $\rho = 2770 \text{ kg/m}^3$. Even though center to center spacing of inclusions for Al 2024 and Al 2124 alloys with T6 temper condition are not provided in the open literature (to the authors' best knowledge), Hahn and Rosenfield [39] provided center to center spacing of inclusions for Al 2024 and Al 2124 alloys with T851 temper condition. Hence, considering the average value of (center to center spacing of inclusions for) Al 2024-T851 and Al 2124-T851 alloys gives a characteristic length of $l_{1,0} \approx 8 \text{ }\mu\text{m}$. Despite the fact that temper condition of the alloy of interest is different than those considered in the prediction of the characteristic length, $l_{1,0} \approx 8 \text{ }\mu\text{m}$ is a reasonable approximation, as it is on the order of inclusion spacing of other 2xxx Al alloys as well, for instance, Al 2014-T6 alloy (see, e.g., [39]).

3.2 Example 2: Tensile mode fracture of Ti–10V–2Fe–3Al (Ti–1023)

Bobbili and Madhu [12] conducted tensile tests on Ti–10V–2Fe–3Al (also called Ti-10-2-3) alloy at four different strain rates as well: 0.01 s^{-1} , 500 s^{-1} , 1000 s^{-1} , 1500 s^{-1} . Again, the specific surface energy density, C_I , is determined for three additional strain rates, i.e., for 5000 s^{-1} , $20,000 \text{ s}^{-1}$, $50,000 \text{ s}^{-1}$, and the approximate fracture strains at these strain rates are calculated by using Johnson–Cook fracture criterion. The expression was given by Bobbili and Madhu [12] as

$$\bar{\varepsilon}_f = \left[-0.04 + 0.46e^{0.21\eta} \right] \left[1 + 0.027 \ln \left(\frac{\dot{\varepsilon}}{\dot{\varepsilon}_0} \right) \right]. \quad (30)$$

Again, Eq. (30) is used to determine the fracture strains only for three stress triaxialities in order to obtain the approximate value of C_I at strain rates beyond 1500 s^{-1} .

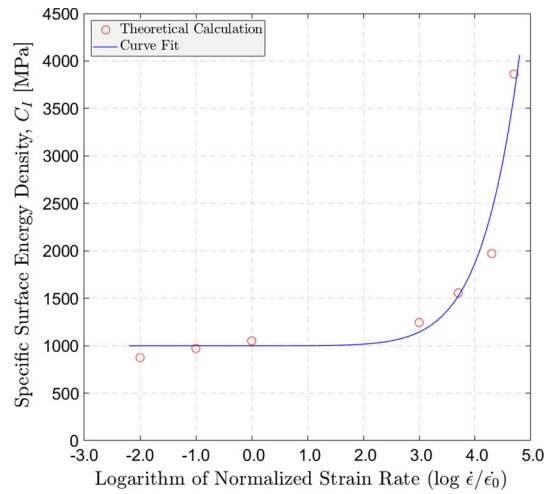


Fig. 2 Specific surface energy density of Al–4.8Cu–1.2Mg alloy for various strain rates

In addition, the following constitutive equation, whose material constants are provided by Bobbili and Madhu [12], is used to predict the flow behavior of Ti–10V–2Fe–3Al alloy

$$\sigma_{\text{eq}} = \left[842 + 754 \varepsilon_{\text{eq}}^{0.42} \right] \left[1 + 0.021 \ln \left(\frac{\dot{\varepsilon}}{\dot{\varepsilon}_0} \right) \right] \quad (31)$$

with the reference strain rate is taken as $\dot{\varepsilon}_0 = 1 \text{ s}^{-1}$.

Mass density of Ti–10V–2Fe–3Al alloy is $\rho = 4650 \text{ kg/m}^3$ [17]. Moreover, the defect spacing (only inclusions and pores that participated in the fracture process are included) of Ti–10V–2Fe–3Al alloy was provided in Figure 15 of Moody et al. [66] for various samples that were subjected to different processing conditions. Taking an average value of these data gives a characteristic length of $l_{1,0} \approx 12 \text{ } \mu\text{m}$.

4 Results and discussion

The specific surface energy densities of Al and Ti alloys of interest for a wide range of strain rates are presented in Figs. 2 and 3, respectively. Red circles are determined using the critical state equation (with actual experimental data or data obtained through Johnson–Cook fracture criterion) and a curve fit of red circles are presented as a blue solid line. The data used for the lowest four strain rates are the experimental data, whereas Johnson–Cook data are used for the remaining three strain rates. The equation of the curve fit (blue solid line) takes the form of $C_I = 999.5 + 2.5 \times 10^{-7} \left[2.86 + \log \left(\frac{\dot{\varepsilon}}{\dot{\varepsilon}_0} \right) \right]^{11.4}$ for the Al–4.8Cu–1.2Mg alloy (see Fig. 2), and $C_I = 1011 + 6.5 \times 10^{-7} \left[2.98 + \log \left(\frac{\dot{\varepsilon}}{\dot{\varepsilon}_0} \right) \right]^{11.6}$ for the Ti–10V–2Fe–3Al alloy (see Fig. 3).

As can be seen from Figs. 2 and 3, the specific surface energy density (hence, the critical effective energy release rate) remains nearly constant at low strain rates. The specific surface energy density for the Al–4.8Cu–1.2Mg and Ti–10V–2Fe–3Al alloys at low strain rates are determined as on the order of $C_I^{\text{Al}} \approx 1000 \text{ MPa}$ and $C_I^{\text{Ti}} \approx 2000 \text{ MPa}$, respectively. These values correspond to critical effective energy release rates of $\Gamma_1^{\text{Al}} \approx 8 \text{ kJ/m}^2$ and $\Gamma_1^{\text{Ti}} \approx 24 \text{ kJ/m}^2$ for Al–4.8Cu–1.2Mg alloy and Ti–10V–2Fe–3Al alloy, respectively. The determined critical effective energy release rates are consistent with the energy release rates of Al and Ti alloys provided by Hahn et al. [38].

On the other hand, the specific surface energy density (hence, the critical effective energy release rate) increases dramatically at high strain rates, that is, the specific surface energy density and the critical effective energy release rate are highly dependent on the loading rate at high strain rates. The trend of increase in critical effective energy release rate with strain rate, particularly at high strain rates, agrees with the results reported in the literature. Both experimental (see, e.g., [71]) and numerical (see, e.g., [70]) studies showed that the effect of loading rate on energy release rate is little at small loading rates, whereas energy release rate is found to increase dramatically at high loading rates. Actually, the second term in Eqs. (18) and (19) explains the reason

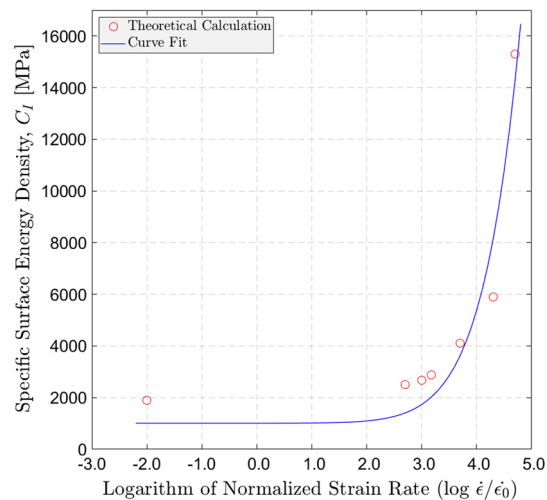


Fig. 3 Specific surface energy density of Ti–10V–2Fe–3Al alloy for various strain rates

behind these observations. As can be seen from these equations, the second term is proportional to square of the strain rate and it does not contribute to the response very much until it approaches on the order of maximum principal stress (σ_1). In other words, the specific surface energy density (hence, the critical effective energy release rate) does not change significantly until a critical strain rate (at which the second term approaches on the order of maximum principal strain) and then increases dramatically as the second term in the critical state equation is proportional to the square of the strain rate. Physically, material rate sensitivity and the material microstructure were found to be the main governors of this response [70]. The critical state equation is in accordance with this finding as well. In the equation, the maximum principal stress (σ_1) represents the material rate sensitivity, whereas the material microstructure is represented by the characteristic length ($l_{1,0}$).

Fracture loci of Al and Ti alloys of interest for three different strain rates are shown in Figs. 4 and 5, respectively. Fracture loci curves for $\dot{\epsilon} = 20,000 \text{ s}^{-1}$ are determined by evaluating the data obtained by Johnson–Cook fracture criterion, whereas the remaining two curves are obtained by evaluating experimental data presented by Bobbili et al. [13] and Bobbili and Madhu [12]. Newton–Raphson method is used to solve the critical state equation.

An interesting observation from Figs. 4 and 5 is that the fracture locus loses its nonlinear characteristic as the strain rate increases and it turns into nearly linear at ultra-high strain rates (the classification of strain rates in this article is based on the classification proposed by Piao et al. [74]) as can be seen from red dash-dot lines. However, determined fracture strains for the highest strain rate considered (i.e., $\dot{\epsilon} = 20,000 \text{ s}^{-1}$) do not agree well with the fracture strains estimated by Johnson–Cook criterion. The main reason for this disagreement is believed to be the fact that Johnson–Cook fracture criterion is an empirical criterion and may not produce accurate results for strain rates much higher than the strain rates used to determine the model parameters. Moreover, proportional loading assumption, neglecting temperature increase and the use of Johnson–Cook constitutive model are believed to slightly contribute to this disagreement as well.

As stated before, proportional loading is not generally the case in actual experiments, and the temperature of the material increases at high loading rates. Nevertheless, neither loading history nor temperature changes throughout loading are considered in the example applications presented here, as no data on the history of stress/strain state were provided by Bobbili et al. [13] and Bobbili and Madhu [12]. However, both loading history and temperature changes should be considered for the proper application of the critical state equation. The values of temperature-dependent terms, particularly σ_1 (i.e., the constitutive equations) and C_I , should be updated accordingly, in every increment. Moreover, the choice of constitutive model is crucial as well, as strain hardening, strain rate, and temperature sensitivity of the material need to be accurately modeled for the appropriate and correct use of the developed fracture criterion.

Furthermore, as Bobbili et al. [13] and Bobbili and Madhu [12] did not provide any data on local strain rates, global strain rates are used for the example applications considered. However, local strain rate can be different than global strain rate and it is location dependent [81]. Therefore, use of local strain rate is suggested for the appropriate application of the proposed criterion.

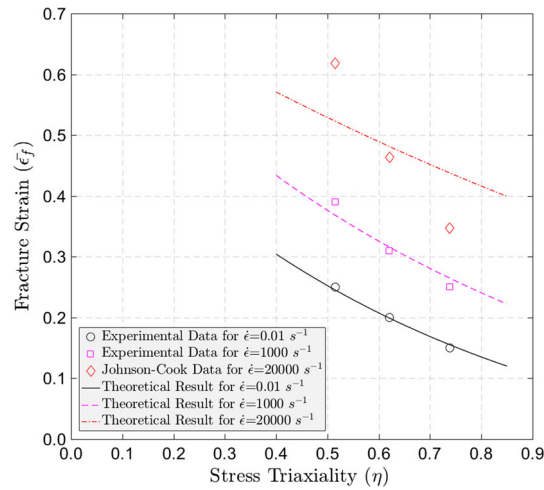


Fig. 4 Fracture locus of Al-4.8Cu-1.2Mg alloy for various strain rates

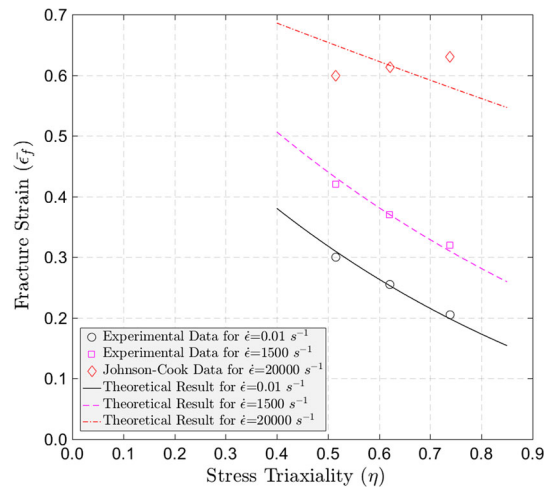


Fig. 5 Fracture locus of Ti-10V-2Fe-3Al alloy for various strain rates

5 Conclusions

The energy balance concept developed by Karr and Akçay [47], which is based on continuum modeling of energy release rates, is further developed to include the effect of dynamic loading into consideration. The formulation introduces a material length scale ($l_{1,0}$) and a material property (C_1) that is a function of strain rate and temperature. C_1 is a material property only in the case of use of a material feature (e.g., a characteristic length) for $l_{1,0}$ such that the stress state within the volume element remains uniform at the continuum scale. Physically, C_1 represents the specific surface energy density as it refers to critical effective energy release rate per unit (characteristic) length [47].

The proposed ductile fracture criterion is implemented into two example applications, Al-4.8Cu-1.2Mg alloy and Ti-10V-2Fe-3Al alloy, whose experimental data were published by Bobbili et al. [13] and Bobbili and Madhu [12]. The fracture loci of these two alloys at various strain rates, and the specific surface energy densities as a function of strain rate are determined. The fracture locus is found to lose its nonlinear characteristic as the strain rate increases, and it turns into nearly linear at ultra-high strain rates (see [74] for the classification of strain rates). Moreover, the specific surface energy densities (hence, the critical effective energy release rates) of the considered alloys are found to be highly dependent on the loading rate, particularly at high strain rates. The trend of increase in critical effective energy release rate with strain rate, particularly at high strain rates, is in accordance with the results reported in the literature (see, e.g., [70,71]). Moreover, determined

critical effective energy release rates of Al–4.8Cu–1.2Mg alloy and Ti–10V–2Fe–3Al alloy are consistent with the energy release rates of Al and Ti alloys provided by Hahn et al. [38].

On the other hand, the fracture criterion proposed in this article is applicable to tensile mode (i.e., Mode I) ductile fracture only. However, in practical applications, fracture may not be pure tensile mode; shear mode fracture, i.e., Mode II fracture (see, e.g., [55,60]), as well as mixed mode fracture (see, e.g., [61]) has been observed commonly at high strain rates. Therefore, development of a companion ductile fracture criterion of shear mode for dynamic loading conditions is vital and an avenue of continuing study.

Acknowledgements The first author would like to thank Dr. Osman Darıcı for his kind help to obtain some articles.

Funding This research did not receive any specific grant from funding agencies in the public, commercial, or not-for-profit sectors.

Compliance with ethical standards

Conflict of interest The authors declare that they have no conflict of interest.

References

1. Amini, M.R., Nemat-Nasser, S.: Micromechanisms of ductile fracturing of DH-36 steel plates under impulsive loads and influence of polyurea reinforcing. *Int. J. Fract.* **162**, 205–217 (2010)
2. Anderson, D., Winkler, S., Bardelcik, A., Worswick, M.J.: Influence of stress triaxiality and strain rate on the failure behavior of a dual-phase DP780 steel. *Mater. Des.* **60**, 198–207 (2014)
3. Andraeus, U., Baragatti, P.: Experimental damage detection of cracked beams by using nonlinear characteristics of forced response. *Mech. Syst. Signal Process.* **31**, 382–404 (2012)
4. Andraeus, U., Baragatti, P., Casini, P., Iacoviello, D.: Experimental damage evaluation of open and fatigue cracks of multi-cracked beams by using wavelet transform of static response via image analysis. *Struct. Control Health Monit.* **24**, e1902 (2017)
5. Asim, U.B., Siddiq, M.A., McMeeking, R.M., Kartal, M.E.: A multiscale constitutive model for metal forming of dual phase titanium alloys by incorporating inherent deformation and failure mechanisms. arXiv preprint [arXiv: 2002.04459](https://arxiv.org/abs/2002.04459) (2020)
6. ASM Handbook Committee: Properties of wrought aluminum and aluminum alloys. ASM Handbook. Volume 2: Properties and Selection: Nonferrous Alloys and Special-Purpose Materials, pp. 62–122. ASM International, Materials Park (2010)
7. Austin, R.A., McDowell, D.L.: A dislocation-based constitutive model for viscoplastic deformation of fcc metals at very high strain rates. *Int. J. Plast.* **27**, 1–24 (2011)
8. Avriel, E., Lovinger, Z., Nemirovsky, R., Rittel, D.: Investigating the strength of materials at very high strain rates using electromagnetically driven expanding cylinders. *Mech. Mater.* **117**, 165–180 (2018)
9. Bai, Y., Wierzbicki, T.: Application of extended Mohr-Coulomb criterion to ductile fracture. *Int. J. Fract.* **161**, 1–20 (2010)
10. Barsoum, I., Faleskog, J.: Rupture mechanisms in combined tension and shear-experiments. *Int. J. Solids Struct.* **44**, 1768–1786 (2007)
11. Benzerga, A.A., Leblond, J.B., Needleman, A., Tvergaard, V.: Ductile failure modeling. *Int. J. Fract.* **201**, 29–80 (2016)
12. Bobbili, R., Madhu, V.: Effect of strain rate and stress triaxiality on tensile behavior of Titanium alloy Ti-10-2-3 at elevated temperatures. *Mater. Sci. Eng. A* **667**, 33–41 (2016)
13. Bobbili, R., Paman, A., Madhu, V.: High strain rate tensile behavior of Al-4.8Cu-1.2Mg alloy. *Mater. Sci. Eng. A* **651**, 753–762 (2016)
14. Børvik, T., Dey, S., Clausen, A.H.: Perforation resistance of five different high-strength steel plates subjected to small-arms projectiles. *Int. J. Impact Eng.* **36**, 948–964 (2009)
15. Børvik, T., Hopperstad, O.S., Berstad, T., Langseth, M.: A computational model of viscoplasticity and ductile damage for impact and penetration. *Eur. J. Mech. A/Solids* **20**, 685–712 (2001)
16. Børvik, T., Hopperstad, O.S., Dey, S., Pizzinato, E.V., Langseth, M., Albertini, C.: Strength and ductility of Weldox 460 E steel at high strain rates, elevated temperatures and various stress triaxialities. *Eng. Fract. Mech.* **72**, 1071–1087 (2005)
17. Boyer, R., Welsch, G., Collings, E.W.: *Materials Properties Handbook: Titanium alloys*. ASM International, Materials Park (1998)
18. Carlouz, T., Dormieux, L., Lemarchand, E.: Thermodynamics of crack nucleation. *Contin. Mech. Thermodyn.* **32**, 1515–1531 (2020)
19. Cayless, R.B.C.: Alloy and temper designation systems for aluminum and aluminum alloys. ASM Handbook. Volume 2: Properties and Selection: Nonferrous Alloys and Special-Purpose Materials, pp. 15–28. ASM International, Materials Park (2010)
20. Charoensuk, K., Panich, S., Uthaisangsuk, V.: Damage initiation and fracture loci for advanced high strength steel sheets taking into account anisotropic behaviour. *J. Mater. Process. Technol.* **248**, 218–235 (2017)
21. Chen, Y., Clausen, A.H., Hopperstad, O.S., Langseth, M.: Stress-strain behaviour of aluminium alloys at a wide range of strain rates. *Int. J. Solids Struct.* **46**, 3825–3835 (2009)

22. Clausen, A.H., Børvik, T., Hopperstad, O.S., Benallal, A.: Flow and fracture characteristics of aluminium alloy AA5083-H116 as function of strain rate, temperature and triaxiality. *Mater. Sci. Eng. A* **364**, 260–272 (2004)
23. Chiyatan, T., Uthaisangsuk, V.: Mechanical and fracture behavior of high strength steels under high strain rate deformation: experiments and modelling. *Mater. Sci. Eng. A* **779**, 139125 (2020)
24. De Angelo, M., Spagnuolo, M., D'Annibale, F., Pfaff, A., Hoschke, K., Misra, A., Dupuy, C., Peyre, P., Dirrenberger, J., Pawlikowski, M.: The macroscopic behavior of pantographic sheets depends mainly on their microstructure: experimental evidence and qualitative analysis of damage in metallic specimens. *Contin. Mech. Thermodyn.* **31**(4), 1181–1203 (2019)
25. Desai, C.S., Sirdiwadane, H.J.: Constitutive laws for engineering materials with emphasis on geologic materials. Prentice-Hall, Upper Saddle River (1984)
26. Dieter, G.E.: *Mechanical Metallurgy*. McGraw-Hill, New York (1986)
27. Dorogoy, A., Rittel, D.: Dynamic large strain characterization of tantalum using shear-compression and shear-tension testing. *Mech. Mater.* **112**, 143–153 (2017)
28. El-Magd, E., Abouridouane, M.: Characterization, modelling and simulation of deformation and fracture behaviour of the light-weight wrought alloys under high strain rate loading. *Int. J. Impact Eng.* **32**, 741–758 (2006)
29. Erice, B., Gálvez, F.: A coupled elastoplastic-damage constitutive model with Lode angle dependent failure criterion. *Int. J. Solids Struct.* **51**, 93–110 (2014)
30. Erice, B., Gálvez, F., Cendón, D.A., Sánchez-Gálvez, V.: Flow and fracture behaviour of FV535 steel at different triaxialities, strain rates and temperatures. *Eng. Fract. Mech.* **79**, 1–17 (2012)
31. Eringen, A.C.: *Mechanics of Continua*. Robert E. Krieger Publishing Company, Melbourne (1980)
32. Fu, J., Xie, W., Zhou, J., Qi, L.: A method for the simultaneous identification of anisotropic yield and hardening constitutive parameters for sheet metal forming. *Int. J. Mech. Sci.* **181**, 105756 (2020)
33. Gambirasio, L., Rizzi, E.: On the calibration strategies of the Johnson-Cook strength model: discussion and applications to experimental data. *Mater. Sci. Eng. A* **610**, 370–413 (2014)
34. Gao, C.Y., Zhang, L.C.: Constitutive modelling of plasticity of fcc metals under extremely high strain rates. *Int. J. Plast.* **32**, 121–133 (2012)
35. Grimsmo, E.L., Clausen, A.H., Aalberg, A., Langseth, M.: Fillet welds subjected to impact loading: an experimental study. *Int. J. Impact Eng.* **108**, 101–113 (2017)
36. Grimsmo, E.L., Clausen, A.H., Langseth, M., Aalberg, A.: An experimental study of static and dynamic behaviour of bolted end-plate joints of steel. *Int. J. Impact Eng.* **85**, 132–145 (2015)
37. Gurson, A.L.: Continuum theory of ductile rupture by void nucleation and growth: part I—yield criteria and flow rules for porous ductile media. *J. Eng. Mater. Technol.* **99**, 2–15 (1977)
38. Hahn, G.T., Kanninen, M.F., Rosenfield, A.R.: Fracture toughness of materials. *Annu. Rev. Mater. Sci.* **2**, 381–404 (1972)
39. Hahn, G.T., Rosenfield, A.R.: Metallurgical factors affecting fracture toughness of aluminum alloys. *Metall. Trans. A* **6**, 653–668 (1975)
40. Hancock, J.W., Mackenzie, A.C.: On the mechanisms of ductile failure in high-strength steels subjected to multi-axial stress-states. *J. Mech. Phys. Solids* **24**, 147–160 (1976)
41. Huang, J., Guo, Y., Qin, D., Zhou, Z., Li, D., Li, Y.: Influence of stress triaxiality on the failure behavior of Ti-6Al-4V alloy under a broad range of strain rates. *Theor. Appl. Fract. Mech.* **97**, 48–61 (2018)
42. Huh, H., Ahn, K., Lim, J.H., Kim, H.W., Park, L.J.: Evaluation of dynamic hardening models for BCC, FCC, and HCP metals at a wide range of strain rates. *J. Mater. Process. Technol.* **214**, 1326–1340 (2014)
43. Johnson, G.R., Cook, W.H.: A constitutive model and data for metals subjected to large strains, high strain rates and high temperatures. In: *Proceedings of the 7th International Symposium on Ballistics*, Hague, pp. 541–547 (1983)
44. Johnson, G.R., Cook, W.H.: Fracture characteristics of three metals subjected to various strains, strain rates, temperatures and pressures. *Eng. Fract. Mech.* **21**, 31–48 (1985)
45. Kabirian, F., Khan, A.S., Pandey, A.: Negative to positive strain rate sensitivity in 5xxx series aluminum alloys: Experiment and constitutive modeling. *Int. J. Plast.* **55**, 232–246 (2014)
46. Kapoor, R., Nemat-Nasser, S.: Determination of temperature rise during high strain rate deformation. *Mech. Mater.* **27**, 1–12 (1998)
47. Karr, D.G., Akçay, F.A.: A criterion for ductile fracture based on continuum modeling of energy release rates. *Int. J. Fract.* **197**, 201–212 (2016)
48. Khan, A.S., Liang, R.: Behaviors of three BCC metal over a wide range of strain rates and temperatures: experiments and modeling. *Int. J. Plast.* **15**, 1089–1109 (1999)
49. Khan, A.S., Liu, H.: A new approach for ductile fracture prediction on Al 2024–T351 alloy. *Int. J. Plast.* **35**, 1–12 (2012a)
50. Khan, A.S., Liu, H.: Variable strain rate sensitivity in an aluminum alloy: response and constitutive modeling. *Int. J. Plast.* **36**, 1–14 (2012b)
51. Khan, A.S., Liu, H.: Strain rate and temperature dependent fracture criteria for isotropic and anisotropic metals. *Int. J. Plast.* **37**, 1–15 (2012c)
52. Khan, A.S., Liu, J., Yoon, J.W., Nambori, R.: Strain rate effect of high purity aluminum single crystals: experiments and simulations. *Int. J. Plast.* **67**, 39–52 (2015)
53. Kim, J.H., Kim, D., Han, H.N., Barlat, F., Lee, M.G.: Strain rate dependent tensile behavior of advanced high strength steels: Experiment and constitutive modeling. *Mater. Sci. Eng. A* **559**, 222–231 (2013)
54. Kim, W.J., Kim, H.K., Kim, W.Y., Han, S.W.: Temperature and strain rate effect incorporated failure criteria for sheet forming of magnesium alloys. *Mater. Sci. Eng. A* **488**, 468–474 (2008)
55. Landau, P., Osovski, S., Venkert, A., Gärtnerová, V., Rittel, D.: The genesis of adiabatic shear bands. *Sci. Rep.* **6**, 37226 (2016)
56. Larsson, R., Razanica, S., Josefson, B.L.: Mesh objective continuum damage models for ductile fracture. *Int. J. Numer. Methods Eng.* **106**, 840–860 (2016)
57. Lee, W.S., Lin, C.F., Liu, T.J.: Impact and fracture response of sintered 316L stainless steel subjected to high strain rate loading. *Mater. Charact.* **58**, 363–370 (2007)

58. Liao, D., Zhu, S.P., Correia, J.A., De Jesus, A.M., Berto, F.: Recent advances on notch effects in metal fatigue: a review. *Fatigue Fract. Eng. Mater. Struct.* **43**, 637–659 (2020)
59. Liu, Y.J., Sun, Q.: A dynamic ductile fracture model on the effects of pressure, Lode angle and strain rate. *Mater. Sci. Eng. A* **589**, 262–270 (2014)
60. Longère, P.: Adiabatic shear banding assisted dynamic failure: some modeling issues. *Mech. Mater.* **116**, 49–66 (2018)
61. Longère, P., Dragon, A.: Dynamic vs. quasi-static shear failure of high strength metallic alloys: experimental issues. *Mech. Mater.* **80**, 203–218 (2015)
62. Majzoobi, G.H., Mahmoudi, A.H., Moradi, S.: Ductile to brittle failure transition of HSLA-100 steel at high strain rates and subzero temperatures. *Eng. Fract. Mech.* **158**, 179–193 (2016)
63. Mohr, D., Marcadet, S.J.: Micromechanically-motivated phenomenological Hosford-Coulomb model for predicting ductile fracture initiation at low stress triaxialities. *Int. J. Solids Struct.* **67**, 40–55 (2015)
64. Molinari, A., Mercier, S., Jacques, N.: Dynamic failure of ductile materials. *Procedia IUTAM* **10**, 201–220 (2014)
65. Molinari, A., Ravichandran, G.: Constitutive modeling of high-strain-rate deformation in metals based on the evolution of an effective microstructural length. *Mech. Mater.* **37**, 737–752 (2005)
66. Moody, N.R., Garrison, W.M., Smugeresky, J.E., Costa, J.E.: The role of inclusion and pore content on the fracture toughness of powder-processed blended elemental titanium alloys. *Metall. Trans. A* **24**, 161–174 (1993)
67. Nahshon, K., Hutchinson, J.W.: Modification of the Gurson model for shear failure. *Eur. J. Mech. A/Solids* **27**, 1–17 (2008)
68. Nguyen, C.T., Oterkus, S., Oterkus, E.: An energy-based peridynamic model for fatigue cracking. *Eng. Fract. Mech.* **241**, 107373 (2020)
69. Nielsen, K.L., Tvergaard, V.: Ductile shear failure or plug failure of spot welds modelled by modified Gurson model. *Eng. Fract. Mech.* **77**, 1031–1047 (2010)
70. Osovski, S., Srivastava, A., Ponson, L., Bouchaud, E., Tvergaard, V., Ravi-Chandar, K., Needleman, A.: The effect of loading rate on ductile fracture toughness and fracture surface roughness. *J. Mech. Phys. Solids* **76**, 20–46 (2015)
71. Owen, D.M., Zhuang, S., Rosakis, A.J., Ravichandran, G.: Experimental determination of dynamic crack initiation and propagation fracture toughness in thin aluminum sheets. *Int. J. Fract.* **90**, 153–174 (1998)
72. Özel, T., Karpuz, Y.: Identification of constitutive material model parameters for high-strain rate metal cutting conditions using evolutionary computational algorithms. *Mater. Manuf. Process.* **22**, 659–667 (2007)
73. Pan, H., Liu, J., Choi, Y., Xu, C., Bai, Y., Atkins, T.: Zones of material separation in simulations of cutting. *Int. J. Mech. Sci.* **115**, 262–279 (2016)
74. Piao, M., Huh, H., Lee, I., Ahn, K., Kim, H., Park, L.: Characterization of flow stress at ultra-high strain rates by proper extrapolation with Taylor impact tests. *Int. J. Impact Eng.* **91**, 142–157 (2016)
75. Placidi, L., Barchiesi, E., Misra, A.: A strain gradient variational approach to damage: a comparison with damage gradient models and numerical results. *Math. Mech. Complex Syst.* **6**, 77–100 (2018a)
76. Placidi, L., Misra, A., Barchiesi, E.: Two-dimensional strain gradient damage modeling: a variational approach. *Z. Angew. Math. Phys.* **69**, 56 (2018b)
77. Placidi, L., Misra, A., Barchiesi, E.: Simulation results for damage with evolving microstructure and growing strain gradient moduli. *Contin. Mech. Thermodyn.* **31**, 1143–1163 (2019)
78. Rittel, D., Weisbrod, G.: Dynamic fracture of tungsten base heavy alloys. *Int. J. Fract.* **112**, 87–98 (2001)
79. Roth, C.C., Mohr, D.: Effect of strain rate on ductile fracture initiation in advanced high strength steel sheets: Experiments and modeling. *Int. J. Plast.* **56**, 19–44 (2014)
80. Rusinek, A., Rodríguez-Martínez, J.A.: Thermo-viscoplastic constitutive relation for aluminium alloys, modeling of negative strain rate sensitivity and viscous drag effects. *Mater. Des.* **30**, 4377–4390 (2009)
81. Shahba, A., Ghosh, S.: Crystal plasticity FE modeling of Ti alloys for a range of strain-rates. Part I: a unified constitutive model and flow rule. *Int. J. Plast.* **87**, 48–68 (2016)
82. Shojaei, A., Voyiadjis, G.Z., Tan, P.J.: Viscoplastic constitutive theory for brittle to ductile damage in polycrystalline materials under dynamic loading. *Int. J. Plast.* **48**, 125–151 (2013)
83. Siddiq, A.: A porous crystal plasticity constitutive model for ductile deformation and failure in porous single crystals. *Int. J. Damage Mech.* **28**, 233–248 (2019)
84. Siddiq, A., Arciniega, R., El Sayed, T.: A variational void coalescence model for ductile metals. *Comput. Mech.* **49**, 185–195 (2012)
85. Siddiq, A., Schmauder, S.: Simulation of hardening in high purity niobium single crystals during deformation. *Steel Grips J. Steel Relat. Mater.* **3**, 281–286 (2005)
86. Sjöberg, T., Kajberg, J., Oldenburg, M.: Fracture behaviour of Alloy 718 at high strain rates, elevated temperatures, and various stress triaxialities. *Eng. Fract. Mech.* **178**, 231–242 (2017)
87. Smerd, R., Winkler, S., Salisbury, C., Worswick, M., Lloyd, D., Finn, M.: High strain rate tensile testing of automotive aluminum alloy sheet. *Int. J. Impact Eng.* **32**, 541–560 (2005)
88. Spagnuolo, M., Barcz, K., Pfaff, A., Dell’Isola, F., Franciosi, P.: Qualitative pivot damage analysis in aluminum printed pantographic sheets: numerics and experiments. *Mech. Res. Commun.* **83**, 47–52 (2017)
89. Sung, J.H., Kim, J.H., Wagoner, R.H.: A plastic constitutive equation incorporating strain, strain-rate, and temperature. *Int. J. Plast.* **26**, 1746–1771 (2010)
90. Tanimura, S., Tsuda, T., Abe, A., Hayashi, H., Jones, N.: Comparison of rate-dependent constitutive models with experimental data. *Int. J. Impact Eng.* **69**, 104–113 (2014)
91. Tvergaard, V.: Influence of voids on shear band instabilities under plane strain conditions. *Int. J. Fract.* **17**, 389–407 (1981)
92. Ulacia, I., Salisbury, C.P., Hurtado, I., Worswick, M.J.: Tensile characterization and constitutive modeling of AZ31B magnesium alloy sheet over wide range of strain rates and temperatures. *J. Mater. Process. Technol.* **211**, 830–839 (2011)
93. Vaz-Romero, A., Rodríguez-Martínez, J.A., Arias, A.: The deterministic nature of the fracture location in the dynamic tensile testing of steel sheets. *Int. J. Impact Eng.* **86**, 318–335 (2015)
94. Voyiadjis, G.Z., Abed, F.H.: Effect of dislocation density evolution on the thermomechanical response of metals with different crystal structures at low and high strain rates and temperatures. *Arch. Mech.* **57**, 299–343 (2005a)

95. Voyiadjis, G.Z., Abed, F.H.: Microstructural based models for bcc and fcc metals with temperature and strain rate dependency. *Mech. Mater.* **37**, 355–378 (2005b)
96. Wang, B., Xiao, X., Astakhov, V.P., Liu, Z.: The effects of stress triaxiality and strain rate on the fracture strain of Ti6Al4V. *Eng. Fract. Mech.* **219**, 106627 (2019)
97. Wierzbicki, T., Bao, Y., Lee, Y.W., Bai, Y.: Calibration and evaluation of seven fracture models. *Int. J. Mech. Sci.* **47**, 719–743 (2005)
98. Yu, X., Li, L., Li, T., Qin, D., Liu, S., Li, Y.: Improvement on dynamic fracture properties of magnesium alloy AZ31B through equal channel angular pressing. *Eng. Fract. Mech.* **181**, 87–100 (2017)
99. Yu, T., Hyer, H., Sohn, Y., Bai, Y., Wu, D.: Structure-property relationship in high strength and lightweight AlSi10Mg microlattices fabricated by selective laser melting. *Mater. Des.* **182**, 108062 (2019)
100. Zener, C., Hollomon, J.H.: Effect of strain rate upon plastic flow of steel. *J. Appl. Phys.* **15**, 22–32 (1944)
101. Zerilli, F.J., Armstrong, R.W.: Dislocation-mechanics-based constitutive relations for material dynamics calculations. *J. Appl. Phys.* **61**, 1816–1825 (1987)
102. Zheng, C., Wang, F., Cheng, X., Liu, J., Fu, K., Liu, T., Zhu, Z., Yang, K., Peng, M., Jin, D.: Failure mechanisms in ballistic performance of Ti-6Al-4V targets having equiaxed and lamellar microstructures. *Int. J. Impact Eng.* **85**, 161–169 (2015)

Publisher's Note Springer Nature remains neutral with regard to jurisdictional claims in published maps and institutional affiliations.